

GT2021-59273

UNSTEADY TURBINE RIM SEALING AND VANE TRAILING EDGE FLOW EFFECTS

Iván Monge-Concepción, Shawn Siroka, Reid A. Berdanier,
Michael D. Barringer, and Karen A. Thole
 Pennsylvania State University
 Department of Mechanical Engineering
 University Park, PA 16802, USA

Christopher Robak
 Pratt & Whitney, a division of
 Raytheon Technologies Corporation
 East Hartford, CT 06118, USA

ABSTRACT

Hot gas ingestion into the turbine rim seal cavity is an important concern for engine designers. To prevent ingestion, rim seals use high pressure purge flow but excessive use of the purge flow decreases engine thermal efficiency. A single stage test turbine operating at engine-relevant conditions with real engine hardware was used to study time-resolved pressures in the rim seal cavity across a range of sealing purge flow rates. Vane trailing edge (VTE) flow, shown previously to be ingested into the rim seal cavity, was also included to understand its effect on the unsteady flow field. Measurements from high-frequency response pressure sensors in the rim seal and vane platform were used to determine rotational speed and quantity of large-scale structures (cells). In a parallel effort, a computational model using Unsteady Reynolds-averaged Navier-Stokes (URANS) was applied to determine swirl ratio in the rim seal cavity and time-resolved rim sealing effectiveness. The experimental results confirm that at low purge flow rates, the VTE flow influences the unsteady flow field by decreasing pressure unsteadiness in the rim seal cavity. Results show an increase in purge flow increases the number of unsteady large-scale structures in the rim seal and decreases their rotational speed. However, VTE flow was shown to not significantly change the cell speed and count in the rim seal. Simulations point to the importance of the large-scale cell structures in influencing rim sealing unsteadiness, which is not captured in current rim sealing predictive models.

NOMENCLATURE

b	Hub radius
C	Chord length
C_p	Coefficient of pressure, $(P - \bar{P})/0.5\rho\Omega^2b^2$
c	Gas concentration
f	Frequency
\dot{m}	Mass flow rate
P	Pressure
PR	Pressure Ratio, P_{in}/P_{out}

r	Radius
Re_x	Axial Reynolds number, $V_x C_x / \nu$
Re_ϕ	Rotational Reynolds number, $\Omega b^2 / \nu$
S	Vane pitch length
s_c	Seal clearance
V	Main gas path velocity
α	Angle between pressure transducers
β	Swirl ratio, $V_\phi / \Omega r$
ϵ_{cc}	Cooling effectiveness, $(c - c_{\infty, in}) / (c_s - c_{\infty, in})$
ν	Kinematic viscosity
Ω	Angular velocity
Ω_D	Disk angular velocity at hub radius, b
Φ	Cooling flow rate, $(\dot{m} / 2\pi s_c \rho \Omega b^2)$
Φ_{min}	Minimum flow parameter to seal a given location
Φ_{ref}	Reference flow rate, Φ_{min} for Location C in the Baseline configuration
ρ	Density

Subscripts and Abbreviations

a	Annulus
in	Inlet conditions
out	Outlet conditions
D	Disk
P	Purge
ref	Generic reference condition
s	Source of cooling flow
x	Axial direction
VTE	Vane trailing edge
ϕ	Tangential direction
∞	Background main gas path level
$-$	Average properties

INTRODUCTION

Increased demand for clean forms of energy paired with global demand for gas turbines in the aviation and power generation industries are drivers for increased turbine efficiency

and lower fuel burn. This increase in turbine efficiency is achieved in part by increases in turbine inlet temperatures and pressure ratios. Current turbine inlet temperatures exceed the melting temperature of the materials in the main gas path, which requires a secondary air flow cooling system, bled from the upstream compressor. One required use of the secondary flow budget is in the rim seal and wheelspace cavity between the stationary and rotating components. This secondary flow, which is high pressure air, is used to seal the cavity from the hot mainstream flow.

While a significant amount of research exists that contribute to a foundational understanding of rim seal ingestion, significant challenges remain to fully understand the complex 3D flow structures in this region, especially in a time-varying sense. Computational fluid dynamics (CFD) is a powerful tool that has been shown in the literature to capture some of the complex flow physics in the rim seal, but models are often limited by geometry simplifications, unknown boundary conditions, and simplified turbulence models required to achieve fully converged solutions [1]. Experimental turbine research facilities have enabled further understanding of ingestion mechanisms, but these research vehicles also often operate using simplified geometries with relatively few capturing important unsteady effects.

The unsteady flow field in the rim seal is influenced in part by a mismatch in tangential velocity between the highly swirled flow in the main annulus and the lower swirled flow in the rim seal cavity. This mismatch in velocity results in fluid instabilities forming at the rim seal interface and are attributed to Kelvin-Helmholtz instability. The Kelvin-Helmholtz based instabilities cause the flow to billow and roll-up developing into large-scale low-pressure structures, referred to as cells, which contribute to driving hot gas ingestion into the rim seal [2].

Using circumferentially-spaced, high-frequency response pressure transducers, these large-scale cell structures have been identified at distinct frequencies below that of the blade passing frequency (BPF) and at a fraction of the rotor speed [3]. These cells can be further characterized by their rotational speed while the number of structures are a function of the purge flow, which will be shown in this paper. Purge flow has been found to influence the presence of these large-scale cell structures in the rim seal cavity. Vane trailing edge (VTE) flow has been found to improve rim sealing in previous studies but the impact on the overall flow field is still not understood [4].

This paper presents time-resolved pressure measurements and Unsteady Reynolds-averaged Navier-Stokes (URANS) predictions of under-platform flows for a single-stage turbine with an engine-representative geometry. Purge flow was varied to study its impact on the large-scale cell rotational speed and quantity. Vane trailing edge flow was also included to determine its influence on the rim seal flow field.

BACKGROUND STUDIES

Hot gas ingestion into the rim seal between stationary and rotating turbine components has been studied experimentally and computationally over the past several decades, as reviewed by

Johnson et al. [5] and Scobie et al. [6]. In general, two primary flow mechanisms contribute to the ingestion process including rotation-induced ingestion caused by disk pumping, and pressure-induced ingestion caused by the vane and blade potential fields. Pressure asymmetries due to the presence of the vanes and blades result in alternating regions of high and low pressure in the main gas path annulus. In these alternating pressure patterns, regions of relative high pressure promote ingestion into the rim seal cavity, and regions of low pressure promote egress from the rim seal cavity.

The majority of the literature on rim seal ingestion includes time-averaged studies that quantify rim sealing effectiveness for varying levels of high-pressure sealing flow injected into the wheelspace cavity. Gradually, ingestion models have been developed based on experimental studies conducted by various research groups. One such model proposes rim sealing predictions through a two-orifice model including one for flow egress and one for flow ingress. The model takes into account inner-cavity rotational effects [7] as well as external main gas path effects [8] to develop theoretical constants that are used to solve the model equations. Although this model has been successfully implemented, there are conditions where the rim sealing effectiveness data trends deviate from such a model, for example an inflection region in the rim sealing effectiveness curve observed in previous studies [9–12]. This inflection region is believed to be caused by the interaction of blade and vane pressure potential fields in the main gas path, as identified by Horwood et al. [13]. In their study, the authors showed that the removal of the spinning blades eliminated the presence of the inflection region, as they have shown in a non-dimensional sealing parameter, Φ_0 . Swirl ratio (β) data in their study showed that in this inflection region there is a noticeable increase in swirl ratio when blades are present. These results clearly indicate ingress of highly swirled flow from the main annulus into the rim seal pointing to unstable shear layers between flow in the main annulus and flow in the rim seal.

Unsteady large-scale structures have been previously studied by various authors using experimental rigs and CFD simulations operating at different turbine conditions and various purge flow rates [2,14,15]. A study by Rabs et al. [2] showed that two parallel flows at different speeds, billow and roll-up due to the velocity mismatch. This rolling and billowing behavior is caused by Kelvin-Helmholtz instability. Rabs et al. also showed that velocity mismatches present between the highly swirled flow in the main annulus and lower swirled flow in the rim seal causes large scale structures to form in the turbine rim seal cavity, which are referred to as cells.

The work by Cao et al. [16] is often credited as one of the first studies to identify the existence of large-scale cell structures in the rim cavity. Through the use of high-fidelity CFD models combined with fast-response pressure measurements, Cao et al. quantified the number of cells in the cavity. The authors found that closing the axial gap between the stator and the turbine rotor prevents ingestion and suppresses the unsteady pressure in the cavity. The CFD study by Jakoby et al. [3] also found the presence of low pressure cells rotating at 80% of the disk speed.

Their study indicated that these cells significantly influence ingestion of main annulus hot gas into the rim seal cavity.

Beard et al. [17] conducted a comprehensive study on unsteady pressure events in the rim cavity without the presence of vanes and blades. They found that the large-scale cells are sensitive to the purge flow rate and rim axial gap. The cell quantity was found to be dependent on sealing flow rate, but the cell speed remained constant at 80% of the disk speed for all sealing flow rates studied. Gao et al. [18,19] conducted computational studies of the geometry presented by Beard et al. [17] using large eddy simulations (LES) and unsteady Reynolds-averaged Navier-Stokes (URANS) simulations. Gao et al. showed that the frequency spectra involved in hot gas ingestion was closely matched to the experiments. LES modeling showed that ingestion can occur on the rotor-side and egress on the stator-side, contrary to conventional ingestion theory [7,8]. Wang et al. [20] used URANS to compute the rim cavity unsteadiness for a single-stage low-speed turbine facility, and found that using a 360-degree domain instead of a sub-sector model provided better agreement with experimental data. Their results showed cell structures in the rim seal caused by shear flow were consistent with areas of low rim sealing effectiveness.

Methodically controlled experiments were performed by Hualca et al. [21] to evaluate the effect of blade and vanes on large-scale unsteady events. Performing experiments with blades showed that at specific flow rates an increase in swirl ratio is observed in the rim seal at the same time a decrease in rim sealing effectiveness is observed. Removal of the blades suppressed this increase in swirl, and a monotonic increase in rim sealing effectiveness was observed as purge sealing flow increases.

Most rim seal studies have focused on varying the purge sealing flow rate and the rim axial gap, but the inclusion of more complex, engine-realistic cooling and geometric features are lacking from the literature. As an example, vane trailing edge (VTE) flow is present in most modern gas turbines, which affects the vane-blade flow interactions. In a study conducted within the same facility as that used in the current paper, Monge-Concepción et al. [4] found the presence of VTE flow in the rim seal region using a CO₂ flow tracing method. At low purge flow rates, the presence of VTE flow in the rim cavity increased, due to low rim seal cavity pressure allowing ingestion into the rim seal. URANS modeling also showed the presence of VTE flow in the rim cavity and showed that part of the VTE flow closest radially to the vane hub partially mixes with main gas path flow prior to ingestion into the rim seal cavity. Siroka et al. [22] used fast-response temperature and pressure sensors in the rim seal of the same test turbine to correlate unsteady events to rim cooling effectiveness. At certain purge flow rates, time-resolved temperatures were out of phase with pressure which indicated ingestion into the rim seal. Temperature sensors showed a decrease in temperature when VTE flow was present in the main gas path, confirming flow migration from the VTE cooling flow into the rim seal. The study also found a direct correlation exists between the unsteadiness and the effectiveness inflection point.

The study presented in this paper expands the understanding of rim sealing effectiveness through detailed time-resolved

measurements showing a comprehensive analysis of the effect of VTE flow. Time-averaged rim cooling effectiveness results are first presented with and without the presence of VTE flow. Time-resolved pressure results are then presented in which the peak frequencies, cell speed, and cell count are all correlated. Although a collection of research exists in the literature for unsteady rim seal phenomena, this paper uniquely represents the first open study analyzing the effect of VTE flow on unsteady pressure phenomena in the rim seal.

EXPERIMENTAL METHODS

The study presented in this paper was performed at Pennsylvania State University within the Steady Thermal Aero Research Turbine (START) Lab. At the center of the lab is an open-loop, continuous-duration test rig with a single-stage turbine designed to operate at engine-relevant Reynolds and Mach numbers using realistic hardware. This facility was designed to study and incorporate improvements in under-platform sealing, cooling technologies, additive manufacturing, and novel instrumentation development. The design of the turbine facility is described in detail by Barringer et al. [23].

Figure 1 shows the main components of the START facility. Two industrial compressors powered by separate 1.1 MW (1500 hp) motors supply compressed air to the turbine main gas path (MGP) and secondary air system, for a combined air flow rate up to 11.4 kg/s (25 lbm/s). Each compressor has the capacity to discharge flow at 480 kPa and 395K (70 psig and 250°F). The compressor discharge air to be used in the turbine main gas path is heated to test condition using a 3.5 MW in-line natural gas heater. The heater is capable of increasing the compressor discharge air temperature from 390 K to 670 K (250°F to 750°F).

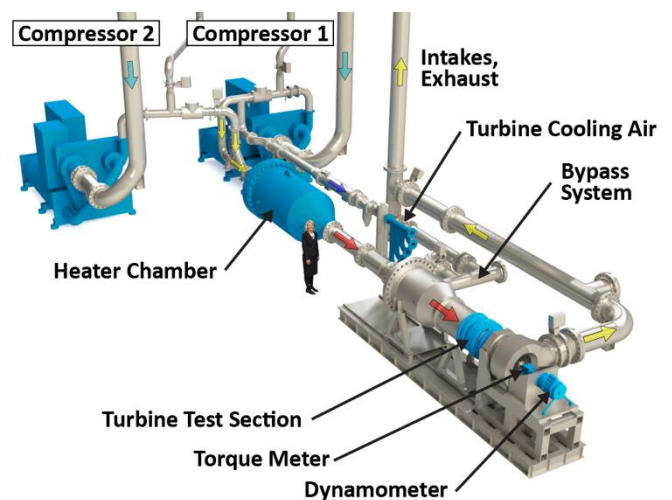


Figure 1. Solid model of the START facility showing the main components.

The secondary air system is supplied by a fraction of the compressor discharge flow. This secondary flow air is thermally conditioned by a shell-and-tube heat exchanger that cools the air

temperature to 273 K (32°F). This secondary air is subsequently distributed to multiple independently controlled and metered cooling flow streams, and then delivered to several locations within the turbine test section.

Figure 2 shows the main gas path air and the secondary air flow capabilities in the test turbine. Three independently controlled secondary air flows are present in the current configuration of the test turbine including: purge flow (e), vane trailing edge flow (g), and tangential on-board injection (TOBI) disk flow (h). The purge flow is delivered axially into the rim seal cavity location (c) through 150 holes equally spaced in the circumferential direction. The VTE flow is delivered through slots in the trailing edge of each turbine vane that span radially from hub to tip. The inner and outer vane plenums (locations (a) and (f)) are isolated to prevent MGP flow migrating into the plenums and vice-versa. Although the turbine has the capability of introducing TOBI flow to the test turbine, TOBI flow was not used in this study.

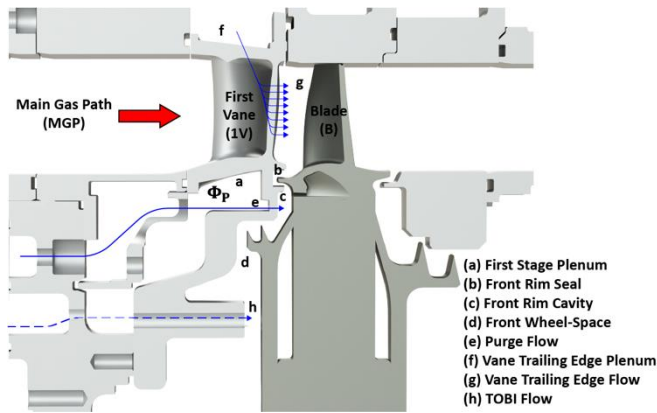


Figure 2. Cross-section diagram showing the turbine main gas path and secondary flow paths.

Facility Instrumentation

For the current study the turbine was operated in a single-stage stator-rotor configuration. Additively manufactured (AM) nickel-alloy vanes were produced using a direct-metal-laser-sintering process to accommodate fast-response pressure and temperature sensors. Additive manufacturing facilitated the installation of custom-made features in the vane to easily accommodate sensors while maintaining airfoil geometry. Previous studies [4,24,25] in the START facility featured similar AM vanes with integral pressure sampling taps to quantify static pressure and rim sealing effectiveness in the under-platform regions. Figure 3(a) shows the locations for the rim seal, rim cavity, and main gas path sensors. Fast-response pressure transducers were installed in locations A (rim seal), E (vane platform), and G (vane tip).

A total of ten high-frequency response, piezo-resistive pressure transducers were installed in the instrumented vane as shown in Figure 3(b). These high-frequency response pressure

transducers exhibit a usable bandwidth that is several times larger than the blade passing frequency, and more than 20 times greater than the primary frequencies of interest for this study. Six transducers were installed in the circumferential direction at location A (identified as A1 through A6) at a radial distance of $r/b = 0.98$. Three transducers were installed at location E (identified as E1 through E3) at a radial distance of $r/b = 0.99$. Additional dimensional details related to the rim seal geometry are summarized in Robak et al. [26]. The last transducer was installed at location G. Each of the transducers installed at location A are circumferentially separated by one-fifth of a vane pitch ($S/5$) while transducers at location E are separated by one half of a vane pitch ($S/2$), where S represents the vane pitch. Multiple circumferentially-distributed sensors installed at each radial location enables the capture of unsteady pressure phenomena propagating tangentially in the cavity. Signals from all fast-response sensors were simultaneously sampled at 100 kHz with analog low-pass filtering to prevent aliasing. A once-per-revolution laser shaft-encoder was installed to enable accurate angular phasing of the sensor signals.

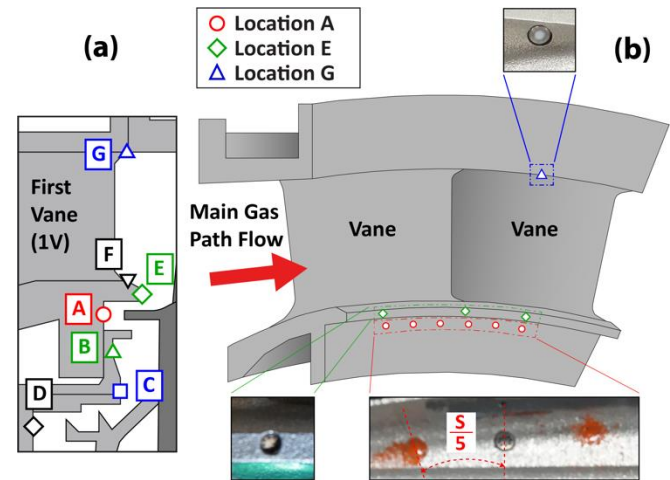


Figure 3. a) Rim seal, rim cavity, and main gas path sensor locations and (b) back view of the instrumented vane showing pressure transducer locations in the radial and circumferential directions.

All pressure transducers were simultaneously calibrated after installation in the vane hardware over a range of pressures and temperatures to examine associated temperature sensitivities. The detailed procedure used in this calibration process is outlined by Siroka et al. [22] using the same instrumented hardware presented for this study.

Rim cooling effectiveness data previously reported by Monge-Concepción et al. [4] showed the importance of vane trailing edge flow. Rim cooling effectiveness, ϵ_{cc} , is defined by Equation 1:

$$\epsilon_{cc} = \frac{c - c_{\infty, in}}{c_s - c_{\infty, in}} \quad (1)$$

where c is the local concentration of the CO₂ seed gas measured at a specific location, c_s is the source concentration of the CO₂ seed gas measured in both the vane under-platform plenum and VTE plenum, and $c_{\infty, \text{in}}$ is the background concentration of CO₂ gas measured at the inlet of the turbine vane in the main gas path.

To determine rim cooling effectiveness, CO₂ was injected into the secondary air (purge and/or VTE flow) to yield a supply CO₂ concentration of 1% within each plenum, respectively. Total pressure probes with Kiel heads were positioned upstream of the turbine vane inlet and were used to sample airflow in the main gas path to determine background inlet CO₂ concentration ($c_{\infty, \text{in}}$). CO₂ concentration was sampled from various radially and circumferentially positioned pressure taps in the vane to determine local concentration (c). By definition, rim cooling effectiveness ranges from zero to one, where a value of zero represents full presence of main gas path flow and a value of one represents full presence of cooling flow in the rim cavity.

Measurement Uncertainty

An uncertainty analysis was performed according to the method outlined by Figliola and Beasley [27] where values shown include bias and precision uncertainty for each parameter. Table 1 shows uncertainties for the turbine operating parameters and pressure transducer data using the maximum facility capability as the reference condition. To reduce uncertainty of the pressure transducer data, each time-resolved data point presented in this study represents 500 disk revolutions of continuous measurements.

Table 1. Measurement Uncertainties

Parameters	Symbol	Total Uncertainty
Main gas path flow rate	$\dot{m}/\dot{m}_{\text{ref}}$	± 0.004
Shaft rotational speed	$\Omega/\Omega_{\text{ref}}$	± 0.001
1.0 stage pressure ratio	$\text{PR}/\text{PR}_{\text{ref}}$	± 0.005
Purge flow rate	$\dot{m}_p/\dot{m}_{p, \text{ref}}$	± 0.018
Pressure coefficient	C_p	± 0.00005
Rim cooling effectiveness	ε_{cc}	± 0.015 to ± 0.05

Turbine Operating Conditions

The turbine operating point for the present study represents the same test conditions described by Monge-Concepción et al. [4], supporting a back-to-back comparison with previously-defined rim cooling effectiveness (ε_{cc}). Flow conditions were held steady throughout the experiment, except for the purge and VTE flow rates, which were varied to determine relative influences on rim seal pressure unsteadiness. Cooling flow rates presented in this paper are scaled cooling flow rates, Φ/Φ_{ref} , where Φ is the cooling flow rate for either purge or VTE flow and Φ_{ref} is the reference flow rate defined as the purge flow rate required to fully seal the rim cavity (Location C in Figure 3(a)). Results are presented using the coefficient of pressure (C_p), non-

dimensional frequency (f/f_D), cell speed (Ω_s), and cell count (N_s). Table 2 shows the turbine operating point throughout all of the test conditions presented in this study.

Table 2. Turbine Operating Conditions

Parameters	Symbol	Value
Vane Inlet Mach Number		0.1
Vane Inlet Reynolds Number	Re_x	1.1×10^5
Blade Inlet Reynolds Number	Re_x	1.1×10^5
Rotational Reynolds Number	Re_ϕ	$4.0 - 9.6 \times 10^6$
Density Ratio	ρ_p/ρ_∞	1.0 – 2.0

To systematically study the effect of purge flow and vane trailing edge flow on rim seal ingestion behavior, two controlled cooling flow configurations were used. Table 3 outlines the two cooling flow configurations named *Baseline* and *Nominal VTE*. By comparing the two configurations, it is possible to study the effect of introducing VTE flow over a range of purge flow rates to examine the relative differences in rim seal unsteadiness.

Table 3. Cooling Flow Configurations

Configuration Name	Φ_p/Φ_{ref}	$\Phi_{\text{VTE}}/\Phi_{\text{ref}}$
Baseline	0.4 – 1.3	0.0
Nominal Vane Trailing Edge	0.4 – 1.3	0.4

COMPUTATIONAL MODEL

An Unsteady Reynolds-averaged Navier-Stokes (URANS) analysis was performed to compare with experimental results and to further understand the time-resolved flow conditions in the rim seal cavity. The computational model represents the full turbine stage with relevant cavity geometries to accurately capture the main gas path and rim seal cavity flow interactions.

A quarter-wheel circumferential sector of the turbine stage geometry was modeled and meshed using commercial software [28]. The mesh was then exported to a commercial CFD code [29] and its URANS solver was used to fully capture unsteady phenomena in the rim seal cavity. The turbulence model used in this study was the $k-\omega$ shear stress transport (SST) model. Details of the meshing process, mesh quality and independence, turbulence model settings, model validations and equations of state are described in further detail by Robak et al. [26].

The flow conditions simulated in the CFD model are the same as those described in the previous section. The simulations were initially converged using a Reynolds-averaged Navier-Stokes (RANS) solver. Time-resolved simulations were then conducted using the URANS solver for a total of five (5) fully converged disk rotations. Monitor points were positioned at the same locations as the pressure transducer sensors in the experimental test article, as shown in Figure 3b. Simulations were considered converged when the pressure amplitudes at the

monitor locations were within 5% of the previous revolution value, as further described by Robak et al. [26].

TIME-AVERAGED RIM COOLING EFFECTIVENESS

Time-averaged results of rim cooling effectiveness were previously reported by Monge-Concepción et al. [4]. Figure 4 shows rim cooling effectiveness (ϵ_{cc}) data for location A versus purge flow rate (Φ_P/Φ_{ref}). Purge flow rate (Φ_P) is nondimensionalized by the reference flow rate (Φ_{ref}), which represents the minimum purge flow rate required to fully seal the rim cavity at location C in Figure 3(a). The *Baseline* flow configuration results are shown using a dashed red line with open symbols, while the *Nominal VTE* flow configuration results are plotted using a solid red line with closed symbols. Figure 4 shows that as the purge flow rate increases, the rim cooling effectiveness at location A in the rim seal also increases for both configurations. As the purge flow rate is increased the air pressure within the rim seal region rises preventing main gas path hot fluid from entering.

The presence of VTE flow in the main gas path results in an improvement in rim cooling effectiveness as shown in Figure 4. The VTE flow closest radially to the vane hub partially mixes with main gas path flow and some of the mixture migrates radially inward into the rim seal resulting in beneficial cooling to the rim seal and rim cavity region. Through the use of fast-response temperature sensors positioned in the rim seal, Siroka et al. [22] showed that the VTE flow presence helps to cool the rim seal. Another important observation at location A in the rim seal is the presence of an inflection region in the purge flow range $0.6 \leq \Phi_P/\Phi_{ref} \leq 0.7$. As discussed in the Background Studies section, this inflection region has been found to be caused by the presence of the blades, as shown by Horwood et al. [13] and Hualca et al. [21], but further studies are required to fully understand the physical mechanisms responsible for this phenomenon.

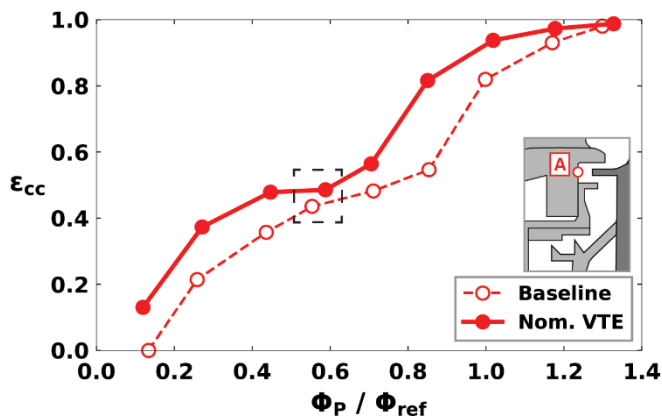


Figure 4. Rim cooling effectiveness at location A in the rim seal for the *Baseline* and the *Nominal VTE* flow configurations from [4].

UNSTEADY PRESSURE MEASUREMENTS

Time-averaged results of rim cooling effectiveness are important to understand the performance of the rim seal, but analysis of time-resolved results point to important unsteady physics in the flow field. Figure 5 shows time-resolved results from CFD simulations for rim cooling effectiveness (primary y-axis, solid-line) and pressure coefficient, C_p , (secondary y-axis, dashed-line) over one full disk rotation for a purge flow rate $\Phi_P/\Phi_{ref} = 0.6$, corresponding to the black dashed box in Figure 4. Local pressures shown in Figure 5 are nondimensionalized to a local coefficient of pressure (C_p) based on the dynamic pressure of purge flow conditions and disk speed.

Results in Figure 5 show that a rise in the local pressure coefficient corresponds to a rise in rim cooling effectiveness, and similarly a decrease in local pressure yields a decrease in rim cooling effectiveness. A total of five distinct peaks can be identified in both curves which are attributed to large-scale, low-pressure cell structures similar to those originally predicted by Cao et al. [16]. Given the matched periodicity between the effectiveness and the pressure curves, the CFD results point to the cells as being a clear contributor of the ingestion process into the rim seal region.

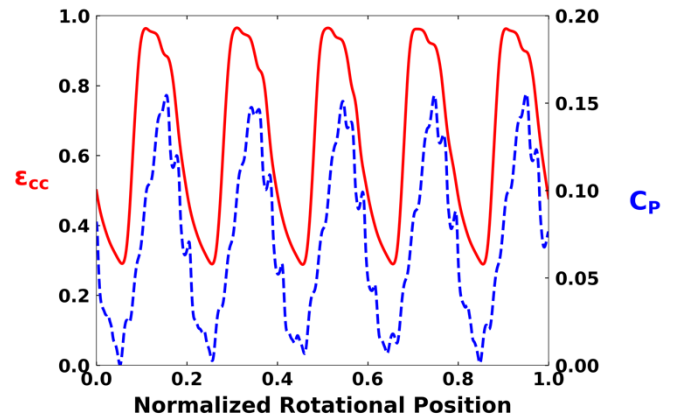


Figure 5. CFD simulation of time-resolved rim cooling effectiveness (ϵ_{cc}) and local nondimensional pressure coefficient (C_p) in the rim seal for a purge flow rate $\Phi_P/\Phi_{ref} = 0.6$.

To improve understanding of the unsteady flow effects that contribute to ingestion, the time-resolved pressure data measured from the high-frequency response sensors were analyzed using Fourier transforms. Previous authors [3,13,15,16] have identified large-scale cell structures rotating in the rim seal at frequencies well below the blade passing frequency (BPF). Figures 6a-d show overlaid Fourier transforms of the measured nondimensional pressure signals, C_p , for both the *Baseline* and the *Nominal VTE* flow configurations at four representative purge flow rates. Each plot in Figures 6a-d shows Fourier transform amplitudes as a function of nondimensional frequency f/f_D where f_D is the frequency of the disk rotation. Experimental data presented in this study was taken over 500 disk revolutions.

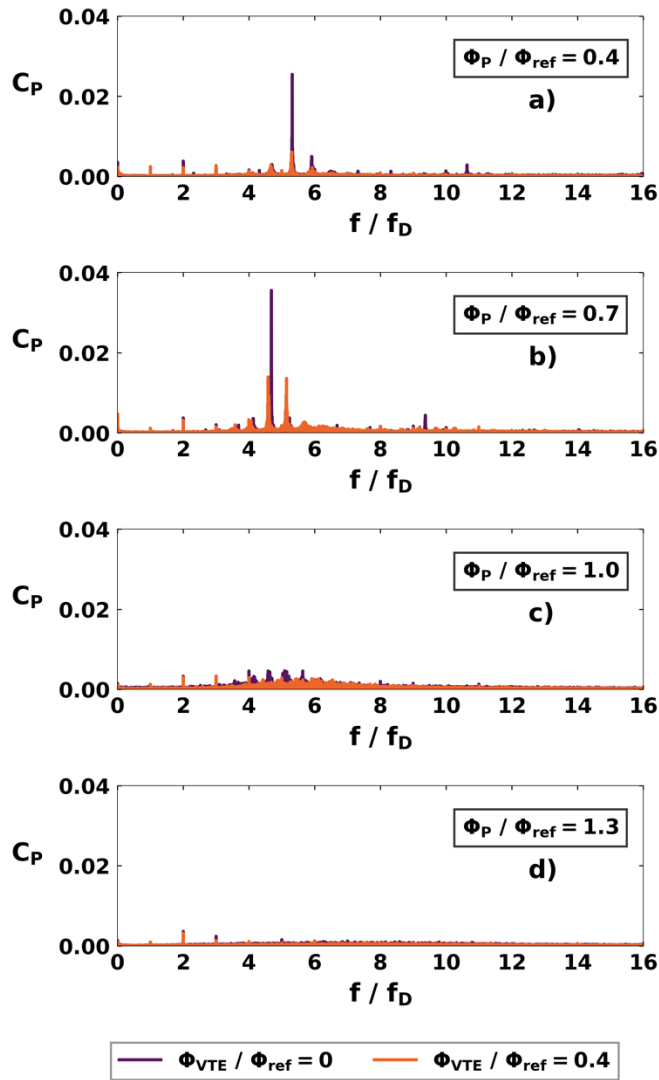


Figure 6. Measured pressure at the rim seal (Location A) plotted in the frequency domain for the *Baseline* and *Nominal VTE* flow configurations. (a) $\Phi_P/\Phi_{ref} = 0.4$; (b) $\Phi_P/\Phi_{ref} = 0.7$; (c) $\Phi_P/\Phi_{ref} = 1.0$; (d) $\Phi_P/\Phi_{ref} = 1.3$.

For most test conditions in Figures 6a-d, a dominant frequency exists in the range of $4 < f/f_D < 6$. Similar dominant frequencies in the same range were identified by Siroka et al. [22] using fast-response pressure and temperature sensors in the rim seal. Using unsteady CFD simulations Jakoby et al. [3] identified dominant pressure frequencies near $f/f_D \approx 2.7$. These frequencies are well below the BPF of the turbine pointing to these unsteady events not being directly related with blade passing events but rather by unsteadiness in the flow field, as suggested by previous authors [2,3,20]. These low frequency peaks are caused by low-pressure cells, and are attributed to Kelvin-Helmholtz instabilities [2], that drive unsteady ingestion into the rim seal cavity. The Kelvin-Helmholtz instabilities develop from a velocity mismatch between the highly swirled

flow in the turbine main gas path annulus and the lower swirled flow in the rim seal cavity. This velocity mismatch causes an unsteady shear layer to form in which the flow billows and rolls forming waves of large-scale low-pressure structures that rotate in the rim seal cavity. The development of Kelvin-Helmholtz instabilities partially drive hot gas ingestion into the rim seal by entraining some of the main gas path hot flow into the large-scale, low-pressure structures as shown by Jakoby et al. [3].

Another result that can be observed from Figures 6a-d, is that the presence of VTE flow (orange colored signal) greatly reduces pressure unsteadiness (lower C_P values), as quantified by the maximum amplitudes across all nondimensional purge flow rates. The VTE flow changes the pressure asymmetries in the annulus by filling in the pressure deficit caused by the vane wake. This additional flow dampens the pressure amplitudes caused by the large-scale structures in the rim seal. Similarly, amplitude dampening of time-resolved temperatures was also identified by Siroka et al. [22] when VTE flow was present in the turbine annulus. For all flow conditions in the current study, the presence of the VTE flow does not change the frequency spectra of the unsteady flow field, but rather dampens the fluctuations. Using URANS simulations, Siroka et al. [22] found that ingested VTE flow slightly increases the swirl ratio (β) in the rim seal. This increase in swirl ratio reduces the velocity gradient between the annulus and the rim seal which suppresses the pressure instability amplitudes.

When purge flow is introduced in the rim cavity at flow rates below the inflection region ($\Phi_P/\Phi_{ref} < 0.4$ in Figure 4), a peak in the C_P amplitude is identified at a nondimensional frequency of approximately $f/f_D \sim 5$ for both the *Baseline* and the *Nominal VTE* configurations, as shown in Figure 6(a). As the purge flow rate is increased and approaches the inflection region, the data in Figure 6(b) indicates that the pressure unsteadiness reaches its maximum amplitude. As the purge flow rate is increased past the inflection region, Figure 6(c-d) shows not only does the pressure amplitude decrease in the rim seal, but multiple peaks appear over a wider range of frequencies from $4 < f/f_D < 12$. This increase in the frequency range is hypothesized to be caused by the increased velocity mismatch between the highly-swirled annulus flow and axially-injected purge flow. Widening of the frequency spectra as purge flow rate increases was similarly identified by Savov et al. [15].

To further understand the unsteady pressure phenomena in the rim seal region, an in-depth analysis was performed to determine the peak frequency of the pressure signal on a per-revolution basis of the disk. The peak frequency f_{peak} is defined as the frequency corresponding to the maximum pressure amplitude during one full disk revolution. Peak frequencies were calculated for each of the individual 500 disk revolutions by splitting the pressure transducer data signals per revolution. Fast Fourier transforms were then performed for each of the revolutions to determine the peak frequency. The results of this analysis are shown in Figure 7, in which the average nondimensional peak frequency f_{peak}/f_D is shown for each purge flow rate for both the *Baseline* and the *Nominal VTE*

configurations, and for both the rim seal and vane platform locations. The individual bars shown in Figure 7 represent the average nondimensional peak frequency (f_{peak}/f_D) for the 500 disk revolutions. Also shown is the calculated variance of the peak frequency, which is the minimum-to-maximum range of the peak frequency during the 500 disk revolutions. Frequencies identified between $1 < f/f_d < 3$ in Figure 6(c-d) were found to be not related to large-scale, low-pressure structures in the rim seal but rather were hypothesized to be caused by engine hardware harmonics (other than vanes and blades).

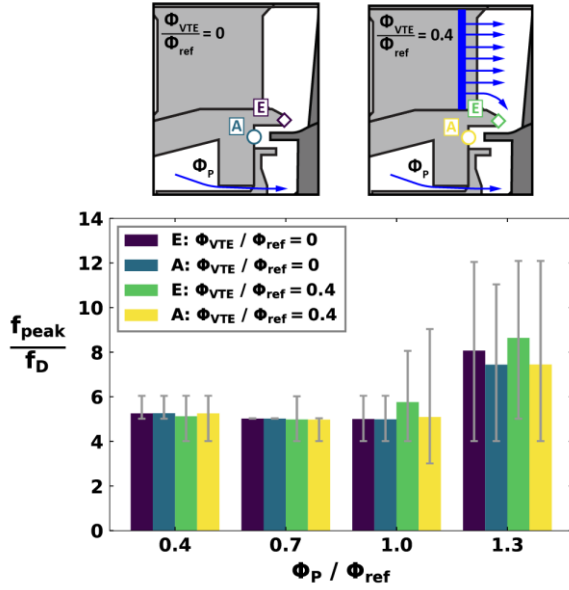


Figure 7. Peak frequency for the *Baseline* and *Nominal VTE* configurations at locations A and E from experiment.

For purge flow rates between $\Phi_P/\Phi_{\text{ref}} = 0.4$ to 1.0, the peak frequency has a small variance as shown in Figure 7. At the inflection point ($\Phi_P/\Phi_{\text{ref}} = 0.7$) where the coefficient of pressure C_p is the highest, the peak frequency variance is the lowest such that the peak frequency does not change per revolution. For purge flow rates above the inflection region, the variance and average peak frequency increase and reach a maximum at the fully sealed condition ($\Phi_P/\Phi_{\text{ref}} = 1.3$). The importance of these peak frequency fluctuations will become more evident as cell speed and cell count are discussed for the different flow configurations in the following section.

Comparison of the peak frequency at the vane platform (location E) and rim seal (location A) shows that the peak frequency has almost no change as flow is ingested from the main gas path annulus to the vane platform and then into the rim seal. This similitude in peak frequency observations suggests that there is a single unsteady cell structure spanning from the platform to the rim seal rather than a pair of two individual structures (one in the platform and one in the rim seal). Overall, a comparison between the *Baseline* and *Nominal VTE* flow configurations shows that the VTE flow dampens the peak

pressure amplitudes throughout all of the purge flowrates in this study.

Examples of both raw and filtered signals from the fast-response pressure transducers in the rim seal are shown in Figure 8. The raw pressure signals are shown for sensors A1, A2, A3, and A6 (location A) over one full disk revolution for the *Baseline* flow configuration with $\Phi_P/\Phi_{\text{ref}} = 0.4$ and $\Phi_{\text{VTE}}/\Phi_{\text{ref}} = 0.0$. To provide additional context, pressure signals in Figure 8 were normalized to a dynamic pressure based on the purge flow conditions and disk speed ($0.5\rho_P\Omega^2b^2$).

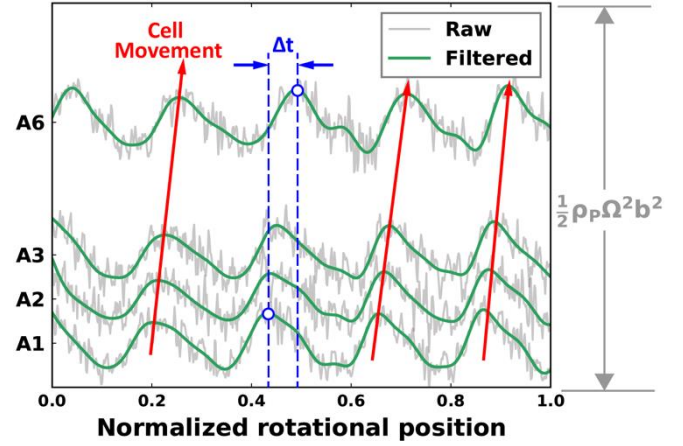


Figure 8. Fast-response pressure data plotted versus normalized rotational position showing raw and filtered signals in the rim seal at a purge flow rate $\Phi_P/\Phi_{\text{ref}} = 0.4$.

The raw data signals shown in Figure 8 include high-frequency fluctuations caused by blade passing events, which are superimposed onto the low-frequency waveforms associated with the rotating large-scale cells. A digital Butterworth low-pass filter (green line) was used with a cutoff frequency of $15f_D$, to more easily visualize the low-frequency oscillations, similar to the approach used by Cameron [30] and Berdanier et al. [31]. The cutoff frequency of $15f_D$ was selected as a point above the primary frequency contributors, including unsteady ingestion patterns, but below the primary blade passing frequency.

Through comparison of the filtered signals in Figure 8, the pressure peak for each subsequent sensor at location A is slightly offset in time (normalized rotation position) from previous sensors as shown by the red arrows in Figure 8. As these unsteady cells in the rim seal rotate tangentially in the direction of the disk rotation, they create alternating pressure fluctuations that are registered by the pressure transducers.

Using two circumferentially spaced transducers, it is possible to calculate the time (Δt) it takes for a fluid cell to pass from one transducer to the next transducer. Using a cross-correlation of the filtered signals between two tangentially separated transducers it is possible to determine the time delay Δt between the two sensor locations. A cross-correlation, or a sliding dot product, is a measure of similarity between data signals from two sensors as a function of their displacement and were used to determine speed and count of the large-scale cells.

CELL SPEED AND CELL COUNT

Fourier transforms of the pressure sensor data support the identification of the different frequencies and amplitudes of the flow cells that promote detrimental main gas flow ingestion into the rim seal. Additional flow characteristics were also determined by using at least two pressure transducers at each radial location to quantify the cell structure tangential speed and count. To calculate these properties, three parameters must be known including the angle between transducers (α), the peak frequency (f_{peak}), and the delay time (Δt) between the peak frequency on one transducer to the next transducer.

A phase analysis to determine the cell speed (Ω_s) and count (N_s) was performed using the methodology described by Beard et al. [17]. Equations 2 and 3 were used to determine the cell tangential speed and count respectively.

$$\Omega_s = \frac{\alpha}{\Delta t} \quad (2)$$

$$N_s = \frac{2\pi f_{\text{peak}}}{\Omega_s} \quad (3)$$

Results presented for both cell speed and count are based on data samples that span 500 disk revolutions. Variance bars, shown as gray lines in Figures 9 and 11, were included in the results to show the minimum-to-maximum range for both cell speed and count. Figure 9 shows the large-scale cell speed (Ω_s) for the rim seal and vane platform for both the *Baseline* and the *Nominal VTE* flow configurations at locations A and E. The cell speed is nondimensionalized by the disk rotational speed (Ω_D). The cell speed shown in Figure 9 is calculated using transducer pairs A1–A6 and E1–E3 which are both separated by exactly one vane pitch. By using these transducer pairs, the pitch-average cell speed and count were determined at for the purge flow rate and VTE flow rates shown in Table 3.

Inspection of the results in Figure 9 shows that an increase of purge flow, regardless of location A or E and VTE flow rate, decreases the cell speed at both radial locations. The cell speed ranges from approximately 80% of the disk speed, at the lowest purge flow, down to near 45% of the disk speed at the highest purge flow rate. These relative cell speeds are consistent to previous experimental and computational studies [16,17,21,32] that report cells rotating at a fraction of the disk speed. In these studies, it was shown cells rotate at speeds of ~80% to ~95% of the disk speed.

Figure 9 shows that the presence of VTE flow has a marginal effect on the cell tangential speed. This means that the flow field interaction between the MGP and rim seal is mostly unchanged such that the VTE flow mostly mixes with the annulus flow. Although there is a slight difference in cell speed between the *Baseline* and *Nominal VTE* configurations, the cell speed minimum-to-maximum range between configurations shows that this change is relatively small. Cell speed minimum-to-maximum range is plotted in gray lines for each purge flow rate, sensor location, and flow configuration. It can be observed that

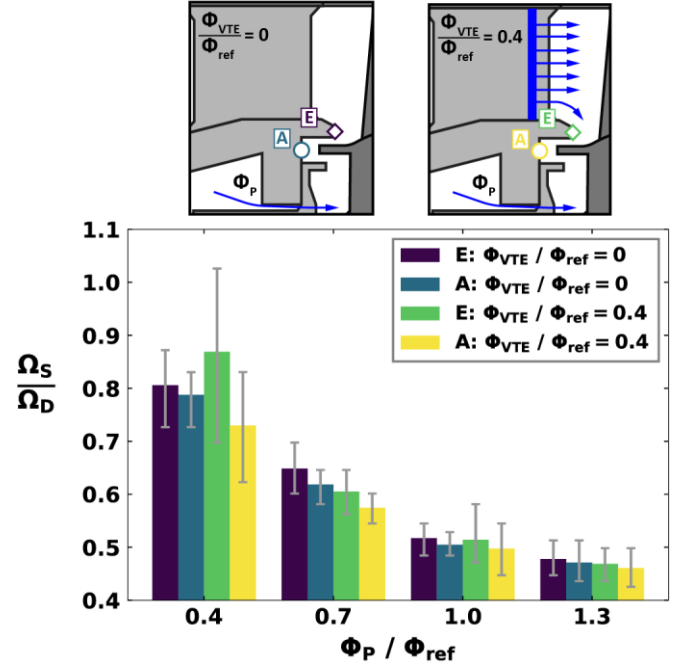


Figure 9. Pitch-average cell speed for the *Baseline* and *Nominal VTE* configurations at locations A and E from experiment.

for a given purge flow rate, the cell speed range (gray lines) changes between ± 0.1 to $\pm 0.2 \Omega_s / \Omega_D$. The cell speed minimum-to-maximum is a direct consequence of changes in the time delay Δt per revolution, since the cell speed is not phase locked to the rotor speed nor the purge flow rate.

Figure 10 shows the radial distribution (r/b) of the average swirl ratio, $\bar{\beta}$, at the tested purge flow rates using CFD. The CFD results presented were taken at the mid-axial plane 50% between the stator wall and the rotor wall as depicted in the inset diagram. For all purge flow rates, the average swirl ratio in the vane platform (location E) is higher than the average swirl ratio in the rim seal (location A). This is caused by the influence of the highly swirled flow in the main gas path annulus which is closest to location E. As the flow is ingested into the rim seal near location A, the flow loses tangential velocity. Additional CFD analysis at axial positions closer to the stationary vane wall will be performed to determine if the predictions more closely match the cell speed experimental data. Figure 10 shows that swirl velocity in the rim seal and rim cavity decreases for all radial locations since the purge flow is injected through holes that angled in the axial direction.

Mathematically, normalized cell speed (Ω_s / Ω_D) and swirl ratio (β) represent similar characteristics. If the cells are moving at a tangential velocity which is equal to the bulk tangential velocity in the rim seal, then the cell speed, Ω_s , is representative of the tangential bulk fluid velocity, V_ϕ . In this case, the cell speed measured by a fast-response pressure sensor can be an indicator of swirl ratio, a critical parameter for rim sealing performance. Additional follow-on work beyond the initial scope

of this study is required to validate such approximations, including an assessment of cell position in the rim seal.

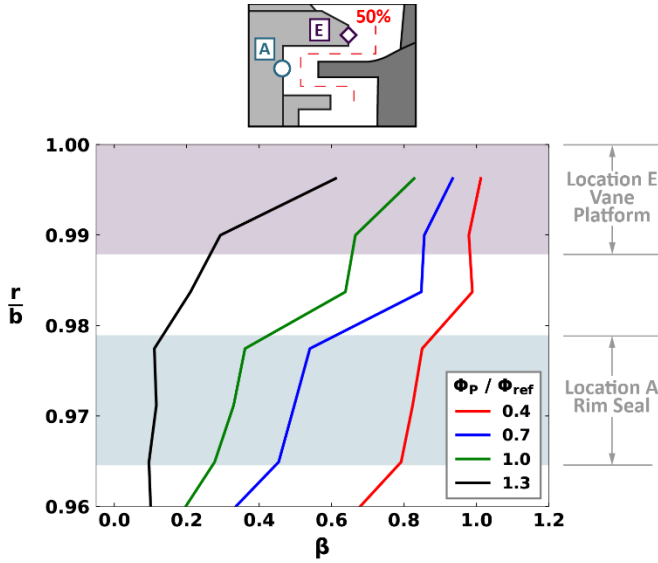


Figure 10. Radial distribution of swirl ratio (β) at various purge flow rates (Φ_P/Φ_{ref}) using URANS CFD simulations.

Pitch-average cell count (N_s) is plotted in Figure 11 at the tested purge flow rates and VTE flow rates in Table 3. It can be seen that as purge flow rate increases, there is an increase in the number of cells present in the platform (location E) and front rim seal region (location A). This result confirms the theoretical trend from Equation 2, that cell speed (Ω_s) has an inverse relation to the number of cells (N_s). The pitch-average cell count increases from approximately 6 cells at the lowest purge flow rate (for both locations A and E), to near 17 cells when the rim seal is fully sealed. It must be noted that when calculating the number of cells present at a specific purge flow rate, the number of cells calculated is not necessarily an integer number. It is hypothesized that the presence of a partial cell is a consequence of individual cells forming and deforming (vortex shedding) in the rim seal as they continuously rotate.

An increase in the cell number occurs due to the purge flow changing the flow field in the rim seal from a highly swirled flow to lower swirl velocity as was shown in Figure 10. This causes a rise in the difference between the swirl velocity in the main gas path annulus and the rim seal, which suggests increased shear flow between the main annulus flow and the rim seal flow. Increased shear flow influences the formation of instabilities. The data indicates that as purge flow increases, more instabilities form in the shear layer which promotes the formation of more cells in the rim seal. Another factor supporting the formation of these cells can be observed in Figure 7 where increases in purge flow increases the variance of f_{peak} . The minimum-to-maximum range of the peak frequency directly correlates to the minimum-to-maximum range of the large-scale structure count present in the rim seal, and is plotted in gray lines in Figure 11. It is evident

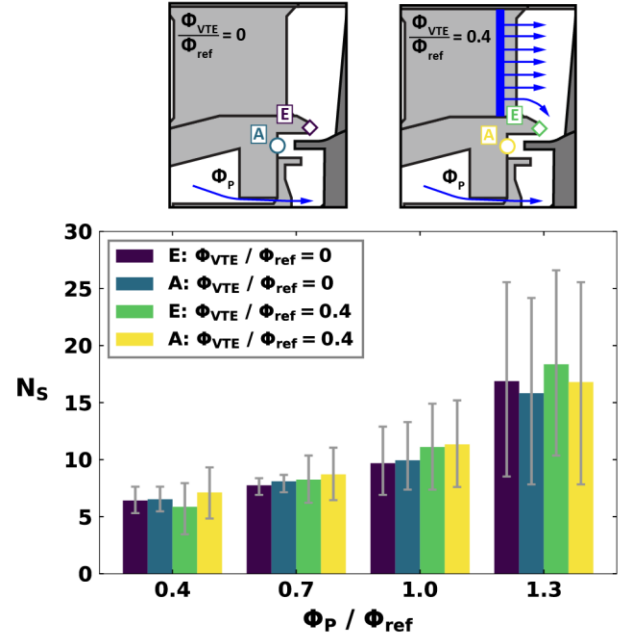


Figure 11. Pitch-average cell count for the *Baseline* and *Nominal* VTE configurations at locations A and E from experiment.

that the instabilities present at higher purge flow rates not only promote the formation of large-scale structures but also increase their variance in the 500 disk revolutions data sample.

The number of large-scale structures present in the rim seal can be clearly observed from the URANS simulations presented in Figures 12 and 13. The CFD results in Figures 12 and 13 were generated from quarter wheel simulations with periodic boundary conditions. Figure 12 shows rim cooling effectiveness (ϵ_{cc}) along with streamlines in the main gas path annulus and rim seal from the rotational frame of reference, while Figure 13 shows the nondimensional coefficient of pressure in the annulus ($C_{p,a}$). Figure 12a shows results for a purge flow rate $\Phi_P/\Phi_{ref} = 0.7$ and VTE flow rate $\Phi_{VTE}/\Phi_{ref} = 0$, and Figure 12b shows a close-up view illustrating one of the large-scale structures in the rim seal. Flow from the highly swirled main annulus encounters lower swirled flow in the rim seal where the velocity mismatch causes the flows to recirculate, in turn forming large-scale structures at the entrance of the rim seal. Inspection of Figure 12b shows that these structures span radially from the vane platform and past the rim seal into the rim cavity. Streamlines show an area of recirculation between the main gas path annulus flow and the rim seal flow. This recirculation zone lowers local rim cooling effectiveness while deeper in the rim cavity shows a high presence of purge flow.

The coefficient of pressure in the rim seal and rim cavity is presented in Figure 13 for a purge flow rate $\Phi_P/\Phi_{ref} = 0.7$ and VTE flow rate $\Phi_{VTE}/\Phi_{ref} = 0$. Figure 13(b) is a close-up view illustrating one of the large-scale structures in the rim seal. Large-scale structures can be observed at locations where the annulus flow coefficient of pressure $C_{p,a}$ is less than 0. This relatively low annulus pressure is a driver of local ingestion into

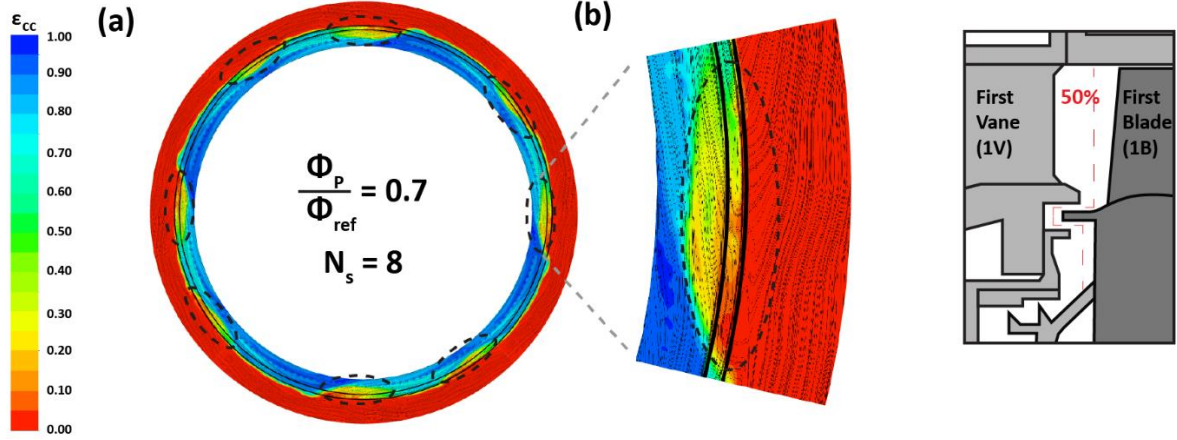


Figure 12. Rim cooling effectiveness (ϵ_{cc}) at a purge flow rate of $\Phi_p/\Phi_{ref} = 0.7$ and VTE flow rate $\Phi_{VTE}/\Phi_{ref} = 0$ depicting full-wheel results (a) and a magnified section of the wheel showing the recirculation zone (b).

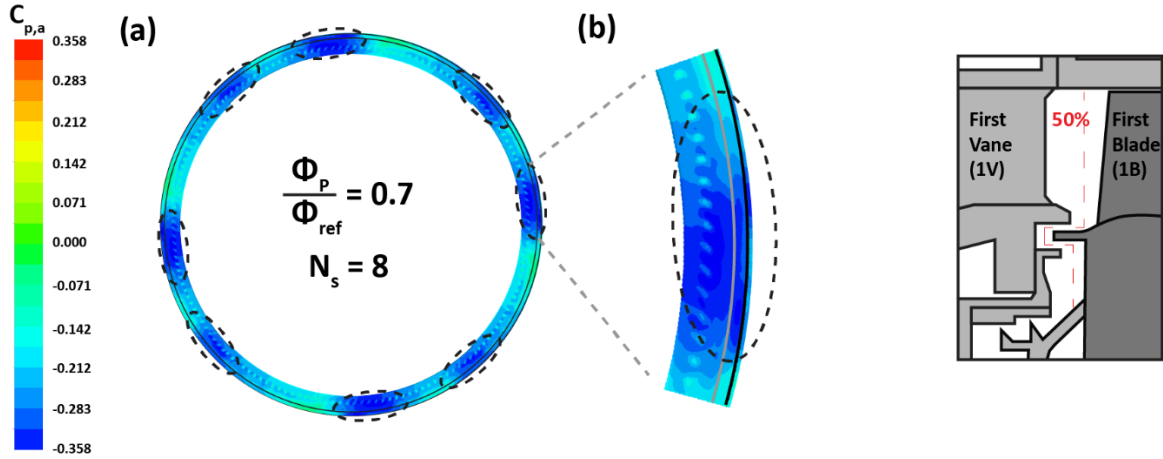


Figure 13. Coefficient of pressure ($C_{p,a}$) at a purge flow rate of $\Phi_p/\Phi_{ref} = 0.7$ and VTE flow rate $\Phi_{VTE}/\Phi_{ref} = 0$ depicting full-wheel results (a) and a magnified section of the wheel showing the recirculation zone (b).

the rim seal which corresponds to the decrease of local rim cooling effectiveness shown previously in Figure 12(b). Closer observation of Figure 13(b) shows that smaller structures are forming around the large-scale structures. It is unclear if these smaller formations are the drivers of the additional peaks observed in the Fourier transforms previously shown in Figure 6. One hypothesis is that the smaller formations are caused by vortex shedding of the larger cells, which can help explain why there is variance in the calculated cell speed and count presented previously in Figures 9 and 11 respectively.

The CFD results presented in this paper provided meaningful insight to further expand understanding of the experimental data. Although 500 disk revolutions were used to determine the minimum-to-maximum ranges in f_{peak} , Ω_s , and N_s for each test condition, only five revolutions of CFD predictions were analyzed due to the high computational cost. It should be noted that although the CFD simulations were validated with experimental data sets [26], some differences between the CFD and experimental results are present due to the complexity of the geometry and flow fields being modeled. Overall, using CFD

simulations aided in accurately capturing the fundamental trends identified by the experimental data.

CONCLUSIONS

A single-stage turbine with real engine hardware was tested at relevant operating conditions to characterize unsteady flow field effects in the rim seal region. Experimental measurements were made using high-frequency response pressure transducers in the vane platform and rim seal, while a URANS numerical model was also used to simulate the highly complex geometries and flow field interactions.

Time-averaged results show an increase in purge flow rate increases the rim cooling effectiveness. Presence of the vane trailing edge flow shows an increase of rim cooling effectiveness across all purge flow rates tested. An inflection region in the rim cooling effectiveness was also found at intermediate purge flow rates with and without the presence of vane trailing edge flow. Time-resolved CFD results in the rim seal region show that the rim cooling effectiveness significantly fluctuates from a fully-

sealed condition to significant ingestion, which in an operating engine would lead to dramatic temperature fluctuations. This finding stresses the importance of the unsteady flow field within the rim seal and the need to better understand the driving mechanisms that influence ingestion.

A frequency domain analysis was performed, and the results revealed the presence of vane trailing edge flow decreases the unsteady pressure amplitudes in the rim seal region across all purge flow rates that were tested. Furthermore, the results show that the unsteady pressure amplitude increases with increasing purge flow rate and reaches a maximum at the purge flow rate corresponding to the inflection region of the rim cooling effectiveness curves. A further increase in purge flow rate past the inflection region decreases the unsteady pressure amplitudes. This rise and fall behavior indicates an important relationship exists between the unsteady flow field and the inflection region.

Unsteady large-scale cells in the rim seal were characterized by their tangential speed and quantity. Results show that purge flow is a significant driver in changing the tangential speed and count of these cells. Increasing the purge flow rate *decreases* the tangential speed of the cells since the purge flow imparts a significant axial momentum to the bulk rim seal flow. Whereas, increasing the purge flow rate *increases* the number of cells present in the rim seal, which is thought to be related to an increase in the quantity of flow instabilities associated with cell formation and deformation.

Results in this study build upon previous findings in the literature on rim cavity instabilities and how they contribute to ingestion. The current study shows the importance in further understanding the nature and impact of the large-scale, low-pressure structures that were found to drive unsteady ingestion into the rim seal region. Critical insights of the unsteady flow mechanisms influencing ingestion can aid engine designers to improve rim seal geometries that suppress the formation of the large-scale cell structures. This work encourages further time-resolved research in the rim seal in order to develop better design tools to mitigate the effects of hot gas ingestion.

ACKNOWLEDGEMENTS

The authors would like to thank Pratt & Whitney and the U.S. Department of Energy National Energy Technology Laboratory for sponsoring research presented in this paper. This paper is based upon work supported by the Department of Energy under Award Number DE-FE0025011.

Disclaimer: "This report was prepared as an account of work sponsored by an agency of the United States Government. Neither the United States Government nor any agency thereof, nor any of their employees, makes any warranty, express or implied, or assumes any legal liability or responsibility for the accuracy, completeness, or usefulness of any information, apparatus, product, or process disclosed, or represents that its use would not infringe privately owned rights. Reference herein to any specific commercial product, process, or service by trade name, trademark, manufacturer, or otherwise does not necessarily constitute or imply its endorsement,

recommendation, or favoring by the United States Government or any agency thereof. The views and opinions of authors expressed herein do not necessarily state or reflect those of the United States Government or any agency thereof."

REFERENCES

- [1] Denton, J. D., 2010, "Some Limitations of Turbomachinery CFD," *Turbo Expo 2010*, Glasgow, UK, GT2010-22540.
- [2] Rabs, M., Benra, F. K., Dohmen, H. J., and Schneider, O., 2009, "Investigation of Flow Instabilities near the Rim Cavity of a 1.5 Stage Gas Turbine," *Turbo Expo 2009*, Orlando, Florida, USA, GT2009-59965.
- [3] Jakoby, R., Zierer, T., Lindblad, K., Larsson, J., Devito, L., Bohn, D. E., Funcke, J., and Decker, A., 2004, "Numerical Simulation of the Unsteady Flow Field in an Axial Gas Turbine Rim Seal Configuration," *Turbo Expo 2004*, Vienna, Austria, GT2004-53829.
- [4] Monge-Concepción, I., Berdanier, R. A., Barringer, M. D., Thole, K. A., and Robak, C., 2020, "Evaluating the Effect of Vane Trailing Edge Flow on Turbine Rim Sealing," *J. Turbomach.*, **142**(August), p. 081001.
- [5] Johnson, B. V., Mack, G. J., Paolillo, R. E., and Daniels, W. A., 1994, "Turbine Rim Seal Gas Path Flow Ingestion Mechanisms," *30th AIAA/ASME/SAE/ASEE Joint Propulsion Conference*, Indianapolis, IN, USA.
- [6] Scobie, J. A., Sangan, C. M., Michael Owen, J., and Lock, G. D., 2016, "Review of Ingress in Gas Turbines," *J. Eng. Gas Turbines Power*, **138**(12), p. 120801.
- [7] Owen, J. M., 2011, "Prediction of Ingestion Through Turbine Rim Seals-Part I: Rotationally Induced Ingress," *J. Turbomach.*, **133**(3), p. 031005.
- [8] Owen, J. M., 2011, "Prediction of Ingestion Through Turbine Rim Seals-Part II: Externally Induced and Combined Ingress," *J. Turbomach.*, **133**(3), p. 031006.
- [9] Gentilhomme, O., Hills, N. J., Turner, A. B., and Chew, J. W., 2003, "Measurement and Analysis of Ingestion Through a Turbine Rim Seal," *J. Turbomach.*, **125**(3), pp. 505–512.
- [10] Scobie, J. A., Sangan, C. M., Owen, J. M., Wilson, M., and Lock, G. D., 2014, "Experimental Measurements of Hot Gas Ingestion through Turbine Rim Seals at Off-Design Conditions," *Proc. Inst. Mech. Eng. Part A J. Power Energy*, **228**(5), pp. 491–507.
- [11] Patinios, M., Scobie, J. A., Sangan, C. M., and Lock, G. D., 2017, "Performance of Rim-Seals in Upstream and Downstream Cavities over a Range of Flow Coefficients," *Int. J. Turbomachinery, Propuls. Power*, **2**(4), p. 21.
- [12] Patinios, M., Ong, I. L., Scobie, J. A., Lock, G. D., and Sangan, C. M., 2018, "Influence of Leakage Flows on Hot Gas Ingress," *Turbo Expo 2018*, Oslo, Norway, GT2018-75071.
- [13] Horwood, J. T. M., Hualca, F. P. T., Wilson, M., Scobie, J. A., Sangan, C. M., and Lock, G. D., 2018, "Unsteady

- Computation of Ingress Through Turbine Rim Seals,” *ASME Turbo Expo 2018*, Oslo, Norway, GT2018-75321.
- [14] Chilla, M., Hodson, H., and Newman, D., 2013, “Unsteady Interaction Between Annulus and Turbine Rim Seal Flows,” *J. Turbomach.*, **135**(5), p. 051024.
- [15] Savov, S. S., Atkins, N. R., and Uchida, S., 2017, “A Comparison of Single and Double Lip Rim Seal Geometry,” *J. Eng. Gas Turbines Power*, **139**(11), p. 112601.
- [16] Cao, C., Chew, J. W., Millington, P. R., and Hogg, S. I., 2004, “Interaction of Rim Seal and Annulus Flows in an Axial Flow Turbine,” *J. Eng. Gas Turbines Power*, **126**(4), pp. 786–793.
- [17] Beard, P. F., Gao, F., Chana, K. S., and Chew, J. W., 2017, “Unsteady Flow Phenomena in Turbine Rim Seals,” *J. Eng. Gas Turbines Power*, **139**(3), p. 032501.
- [18] Gao, F., Chew, J. W., Beard, P. F., Amirante, D., and Hills, N. J., 2017, “Numerical Studies of Turbine Rim Sealing Flows on a Chute Seal Configuration,” *Proceedings of 12th European Conference on Turbomachinery Fluid Dynamics & Thermodynamics*, ETC2017-284.
- [19] Gao, F., Poujoi, N. P., Chew, J. W., and Beard, P. F., 2018, “Advanced Numerical Simulation of Turbine Rim Seal Flows and Consideration for RANS Turbulence Modelling,” *Turbo Expo 2018*, Oslo, Norway, GT2018-75116.
- [20] Wang, C.-Z., Mathiyalagan, S. P., Johnson, B. V., Glahn, J. A., and Cloud, D. F., 2014, “Rim Seal Ingestion in a Turbine Stage From 360 Degree Time-Dependent Numerical Simulations,” *J. Turbomach.*, **136**(3), p. 031007.
- [21] Hualca, F. P. T., Horwood, J. T. M., Sangan, C. M., Lock, G. D., and Scobie, J. A., 2019, “The Effect of Vanes and Blades on Ingress in Gas Turbines,” *TurboExpo 2019*, Phoenix, Arizona, GT2019-90987.
- [22] Siroka, S., Monge-Concepción, I., Berdanier, R. A., Barringer, M. D., and Thole, K. A., 2021, “Correlating Cavity Sealing Effectiveness to Time-Resolved Rim Seal Events in the Presence of Vane Trailing Edge Flow,” *Turbo Expo 2021*, Virtual, Online, GT2021-59285.
- [23] Barringer, M. D., Coward, A., Clark, K. P., Thole, K. A., Schmitz, J., Wagner, J., Alvin, M. A., Burke, P., and Dennis, R., 2014, “The Design of a Steady Aero Thermal Research Turbine (START) for Studying Secondary Flow Leakages and Airfoil Heat Transfer,” *ASME Turbo Expo 2014*, Dusseldorf, Germany, GT2014-25570.
- [24] Clark, K., Johnson, D., Thole, K. A., Robak, C., Barringer, M. D., and Grover, E., 2018, “Effects of Purge Flow Configuration on Sealing Effectiveness in a Rotor–Stator Cavity,” *J. Eng. Gas Turbines Power*, **140**(11), p. 112502.
- [25] Berdanier, R. A., Thole, K. A., Knisely, B. F., Barringer, M. D., Grover, E. A., and Monge-Concepción, I., 2019, “Scaling Sealing Effectiveness in a Stator–Rotor Cavity for Differing Blade Spans,” *J. Turbomach.*, **141**(5), p. 051007.
- [26] Robak, C., Faghri, A., and Thole, K. A., 2019, “Analysis of Gas Turbine Rim Cavity Ingestion with Axial Purge Flow Injection,” *Turbo Expo 2019*, Phoenix, Arizona, USA, GT2019-91807.
- [27] Figliola, R. S., and Beasley, D. E., 2014, *Theory and Design for Mechanical Measurements*, John Wiley & Sons, Inc., USA.
- [28] Siemens PLM Software, 2017, “STAR-CCM+ 11.06,” Plano, TX.
- [29] ANSYS, 2017, “ANSYS Fluent 18.2,” Canonsburg, PA.
- [30] Cameron, J. D., 2007, “Stall Inception in a High-Speed Axial Compressor,” Univ. of Notre Dame.
- [31] Berdanier, R. A., Smith, N. R., Young, A. M., and Key, N. L., 2018, “Effects of Tip Clearance on Stall Inception in a Multistage Compressor,” *J. Propuls. Power*, **34**(2), pp. 308–317.
- [32] Horwood, J. T. M., Hualca, F. P., Wilson, M., Scobie, J. A., Sangan, C. M., Lock, G. D., Dahlqvist, J., and Fridh, J., 2020, “Flow Instabilities in Gas Turbine Chute Seals,” *J. Eng. Gas Turbines Power*, **142**(2), p. 021019.